

# **Tau Neutrinos in IceCube**

## **Dissertation**

zur Erlangung des akademischen Grades  
doctor rerum naturalium  
(Dr. rer. nat.)

im Fach: Physik  
Spezialisierung: Experimentalphysik

eingereicht an der  
Mathematisch-Naturwissenschaftlichen Fakultät  
der Humboldt-Universität zu Berlin

von

**Neha Lad M. Sc.**

geboren am 18. April 1995

Präsidentin der Humboldt-Universität zu Berlin  
Prof. Dr. Julia von Blumenthal

Dekanin der Mathematisch-Naturwissenschaftlichen Fakultät  
Prof. Dr. Caren Tischendorf

**Copyright Notice**

This book is released into the public domain using the CC-BY-4.0 code.

To view a copy of the CC-BY-4.0 code, visit:

<https://creativecommons.org/licenses/by/4.0/>

**Colophon**

This document was typeset with the help of KOMA-Script and L<sup>A</sup>T<sub>E</sub>X using the open-source kaobook template class.

The source code of this thesis is available at:

[https://github.com/LeanderFischer/phd\\_thesis](https://github.com/LeanderFischer/phd_thesis)

# Abstract

In icecube, we have many neutrinos, select some very high energy ones, spend 1 year with them to group them in three flavour categories. I guess we will learn something about where they came from by doing this. Pretty normal stuff, not at all racist.



# Zusammenfassung

Im IceCube haben wir viele Neutrinos, von denen wir einige mit sehr hoher Energie auswählen, verbringen 1 Jahr mit ihnen, um sie in drei Geschmackskategorien einzuteilen. Ich vermute, dass wir auf diese Weise etwas darüber erfahren, woher sie kommen. Ziemlich normales Zeug, ganz und gar nicht rassistisch.



# Contents

<b>Abstract</b>	<b>iii</b>
<b>Zusammenfassung</b>	<b>v</b>
<b>Contents</b>	<b>vii</b>
<b>1 Event Sample,(Re)construction and Particle Identification</b>	<b>1</b>
1.1 Monte Carlo Simulation . . . . .	1
1.1.1 Icecube simulation chain . . . . .	1
1.1.2 SnowStorm Simulation . . . . .	5
1.2 High Energy Starting Event (HESE) sample . . . . .	6
1.3 Maximum Likelihood Event Reconstruction . . . . .	8
1.4 Particle Identification of High Energy Neutrinos . . . . .	10
1.4.1 Reclassification of PeV Double Cascades . . . . .	14
1.4.2 Tau Polarisation . . . . .	15
1.4.3 Glashow Cross-Section correction . . . . .	15
1.5 Influence of South Pole Ice properties on Double Cascades Reconstruction . . . . .	16
 <b>APPENDIX</b>	 <b>19</b>
<b>Figures</b>	<b>21</b>
<b>Tables</b>	<b>23</b>
<b>Bibliography</b>	<b>25</b>





# Event Sample,(Re)construction and Particle Identification

# 1

In the previous chapters, high-energy neutrino interactions within IceCube were discussed, focusing on how the secondary particles generated from these interactions propagate through the ice. From this, one could deduce that different neutrino flavours can create distinct morphological patterns due to the variety of charged particles produced in the interaction processes. As mentioned in Section ??, these morphological signatures are crucial in identifying the neutrino flavour, although it becomes particularly challenging in the case of tau neutrino-induced double cascade events. Apart from the complexities of reconstruction, another critical aspect is the selection of astrophysical neutrinos from the overwhelming background of atmospheric muons and neutrinos.

In this chapter, the high-energy neutrino sample used for the analysis presented in this thesis will be detailed, along with the reconstruction method used to identify the particles based on the event's morphology. The chapter will begin with a general overview of the simulation chain in IceCube, followed by a brief overview of the SnowStorm simulations used for the analysis. Lastly, the chapter will discuss the influence of the South Pole ice model on reconstructed double cascade events.

<b>1.1 Monte Carlo Simulation .</b>	<b>1</b>
1.1.1 Icecube simulation chain .	1
1.1.2 SnowStorm Simulation . .	5
<b>1.2 High Energy Starting Event (HESE) sample . . .</b>	<b>6</b>
<b>1.3 Maximum Likelihood Event Reconstruction . . .</b>	<b>8</b>
<b>1.4 Particle Identification of High Energy Neutrinos .</b>	<b>10</b>
1.4.1 Reclassification of PeV Double Cascades . . . . .	14
1.4.2 Tau Polarisation . . . . .	15
1.4.3 Glashow Cross-Section correction . . . . .	15
<b>1.5 Influence of South Pole Ice properties on Double Cascades Reconstruction</b>	<b>16</b>

## 1.1 Monte Carlo Simulation

The hunt for astrophysical neutrino interactions in the IceCube detector is conducted without access to actual data, a method known as **blind analysis**, which was also followed for the analysis presented in this thesis. To develop the selection (rejection) criteria for signal (background) events, and their light yield reconstruction, simulated events are used.<sup>1</sup> By comparing the distribution of an observable quantity between simulated and real data events, conclusions can be drawn about the detected neutrino population. Hence, simulating how IceCube responds to neutrinos and other particles is essential for comprehending the collected data.

1: In some cases, typically during the development phase of the analysis sample, selection cuts are validated on small subset (10%) of the experimental data, known as *the burn sample*.

### 1.1.1 Icecube simulation chain

An event simulation in IceCube is based on the commonly used Monte Carlo methods. The simulation framework covers all stages, from the generation and propagation of a primary particle to the emission and propagation of Cherenkov light, and finally, the digitized waveforms recorded by all hit DOMs in IceCube.

#### Particle Generation

The IceCube simulation begins with a *particle generator* that simulates a flux of particles hitting the detector. The primary particle can be a neutrino or a cosmic ray particle reaching Earth's atmosphere. Neutrinos may reach the detector directly, while cosmic rays interact with the

nuclei in the atmosphere to produce a shower of particles, from which muons and neutrinos can reach the detector by propagating through ice, forming the so-called atmospheric neutrino and atmospheric muon background.

[1]: Gazizov et al. (2005), *ANIS: High energy neutrino generator for neutrino telescopes*

2: The interaction weight is a probability that a neutrino will make one interaction within a detection volume.

The neutrino generator software, NuGen, is based on the ANIS (All Neutrino Interaction Simulation) framework [1]. NuGen prepares a primary neutrino and propagates it through the Earth, simulating any interactions with Earth's matter if they occur along the way. For neutrinos that reach the detector, an interaction is forced within this volume. Each of these neutrinos that are forced to interact are assigned an interaction weight<sup>2</sup>, which will be further used in assigning a weight to it. Since there's no difference between atmospheric or astrophysical neutrino interactions in ice, these weights can then be used to generate expected event rate for any a specific flux (see below for weight calculations). Neutrinos and antineutrinos, along with all neutrino flavours, are typically generated in equal proportions during simulation, i.e.,  $\nu : \bar{\nu} = 1 : 1$  and  $\nu_e : \nu_\mu : \nu_\tau = 1 : 1 : 1$ .

As these injected neutrinos propagate through the Earth, they may interact with matter in several ways. Supported interactions include charged current (CC) interactions, which produce charged leptons and hadronic/electromagnetic showers; neutral current (NC) interactions, which yield a secondary neutrino and a hadronic shower; and Glashow Resonance (GR) interactions for  $\bar{\nu}_e$ , which generate a hadronic cascade, charged leptons, and neutrinos based on the W-boson decay branching ratio. Following an interaction, NuGen generates secondary particles, but any charged particles or showers are absorbed by the Earth and do not continue propagating. In CC interactions, all secondary particles are absorbed, ending the simulation at the interaction point. However, NC and GR interactions can produce secondary neutrinos, which are then propagated from the interaction point to the IceCube detector. If multiple neutrinos arrive at the detector, NuGen randomly selects one for interaction, as the probability of multiple simultaneous interactions is extremely low. The chosen neutrino will undergo a single interaction within the detection volume, with supported interactions being CC, NC, and GR.

[2]: Heck et al. (1998), *CORSIKA: A Monte Carlo code to simulate extensive air showers*

[3]: Santen (2014), *Neutrino Interactions in IceCube above 1 TeV: Constraints on Atmospheric Charmed-Meson Production and Investigation of the Astrophysical Neutrino Flux with 2 Years of IceCube Data taken 2010–2012*

To generate atmospheric muons, an adapted version of CORSIKA [2] is used to simulate the production of muons resulting from cosmic ray showers in the Earth's atmosphere. This process begins with a primary particle, typically a nucleus, initiating a cascading shower of particles upon interaction with the atmosphere. Only neutrinos and muons from these showers are capable of reaching the detector. Since we can already use the produced neutrinos from NuGen to account for atmospheric contributions, only the muons generated in the showers are transmitted to the detector. The software allows for event weighting based on various cosmic ray models. CORSIKA is currently the exclusive software capable of producing muon bundles, which are large numbers of muons originating from the same cosmic ray shower. However, a major limitation of CORSIKA is its computational expense, as it propagates all particles from a cosmic ray shower, most of which are undetectable in a sub-surface detector like IceCube. To address this drawback, MUONGUN [3] was developed to simulate single muons more efficiently and economically by generating them directly around the detector volume. In the context of

HESE dataset, used in the analysis presented in this thesis (which will be discussed in Section 1.2), the primary background arises from single muons, as muon bundles produce a more continuous light deposition, resulting in a higher likelihood of being identified as background.

Since flux models more complex than a simple power law are often required, NuGen simulations can be re-weighted to match any arbitrary flux. A weight is assigned to each event that reflects the ratio between the desired flux  $n_{\text{expected}} = \Phi(E)$  and the generated fluence of neutrinos. The generated fluence can be expressed as,

$$n_{\text{generated}} = \frac{N(E)}{\Omega A_{\perp}} \quad (1.1)$$

where  $A_{\perp}$  is the projected area of the detection surface for each neutrino, and  $\Omega$  is the solid angle covered by the simulation, typically  $4\pi$  for neutrinos coming from the entire sky.  $N(E)$  represents the energy distribution of simulated neutrinos, which, for a power-law distribution with  $N_0$  events and a power-law index  $\gamma$ , spanning from energy  $E_{\text{min}}$  to  $E_{\text{max}}$ , is given by,

$$N(E) = \frac{N_0 E^{-\gamma}}{\int_{E_{\text{min}}}^{E_{\text{max}}} E^{-\gamma} dE} \quad (1.2)$$

Here,  $N_0$  refers to the number of neutrino or antineutrino events, and not the total, when separate fluxes for neutrinos and antineutrinos are known. This implies that  $N_0$  represents half of the total number of events generated for each neutrino flavour. Finally, accounting for the interaction weight, the total weight assigned to each neutrino (in units of Hz) is,

$$\begin{aligned} w &= w_{\text{int}} \frac{n_{\text{expected}}}{n_{\text{generated}}} \\ &= w_{\text{int}} \frac{A_{\perp} \Omega \Phi(E)}{N(E)} \end{aligned} \quad (1.3)$$

By summing these weights over all simulated events that pass the event selection, the expected event rate for any desired flux model can be calculated.

## Secondary Charged Particle Propagation

Once a particle interaction occurs, the next step is to generate and propagate secondary particles through the ice. Depending on their nature, these secondary particles may undergo further interactions within the ice, with some of them producing detectable Cherenkov light in the detector volume (see Section ?? for details). Both atmospheric muons from air showers and secondary leptons, such as electrons, muons, and taus from CC neutrino interactions, are propagated through the ice after they are produced. The software used for lepton propagation is called PROPOSAL (Propagator with Optimal Precision and Optimized Speed for All Leptons) [4] and is based on the previous implementation MMC (Muon Monte Carlo) [5]. The lepton production is simplified by assuming that the emission

[4]: Koehne et al. (2013), *PROPOSAL: A tool for propagation of charged leptons*

[5]: Chirkin et al. (2004), *Propagating leptons through matter with Muon Monte Carlo (MMC)*

[6]: Voigt (2008), *Sensitivity of the Ice-Cube detector for ultra-high energy electron-neutrino events*

[7]: R  del et al. (2013), *Calculation of the Cherenkov light yield from electromagnetic cascades in ice with Geant4*

[8]: R  del et al. (2012), *Calculation of the Cherenkov light yield from low energetic secondary particles accompanying high-energy muons in ice and water with Geant 4 simulations*

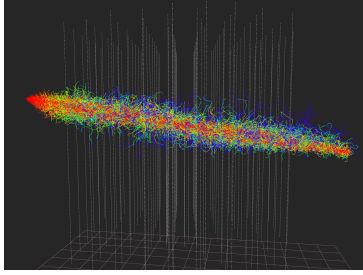


**Figure 1.1:** Light emission pattern of a simulated muon track event, using the direction propagation program CLSim. The colored lines show individual photon paths through ice, with red indicating earlier and blue indicating later compared to an unscattered photon. Figure taken from [9]

#### CLSim

[10]: Chirkin (2013), *Photon tracking with GPUs in IceCube*

3: Three for the source position, three for the DOM position, two for the light source orientation, and one for time.

[11]: Usner (2018), *Search for Astrophysical Tau-Neutrinos in Six Years of High-Energy Starting Events in the IceCube Detector*

angle is aligned with the incident angle of the primary particle, and that it travels at the speed of light, which are both reasonable assumptions above the energy threshold of 100 GeV. The various propagation effects of different particle types and energies, as described in ??, are taken care of by PROPOSAL. In particular, highly energetic muons are simulated to have long tracks that are predominantly characterized by stochastic energy losses. Electromagnetic and hadronic cascades, as described in Section ??, are simulated by CMC (Cascade Monte Carlo) [6]. It generates individual particle showers by randomly sampling energy losses from the energy-dependent shower parametrization and also takes the LPM-effect (see Section ??) into account. The shower parametrizations have been determined by fitting the Cherenkov light yield for a full shower simulation using GEANT4 (Geometry And Tracking) [7, 8].

### Photon Propagation

Once all primary and secondary particles have traversed the detector, the next phase of the simulation process involves the emission and propagation of Cherenkov photons from all visible particles or energy losses (as discussed in Section ??). The number of Cherenkov photons is proportional to the combined track length of all charged particles, and the refraction index of ice. Individual photon propagation is traced through an OpenCL-based photon-tracking simulation (as shown in Figure 1.1), known as CLSim [CLSim], derived from *Photon Propagation Code* (PPC) [10]. The SPICE models (as detailed in Section ??) are used to describe the scattering and absorption of photons. Each photon is tracked through multiple scatterings until it either reaches the collection area of a DOM or, more often, is absorbed. CLSim harnesses GPUs for photon propagation due to their efficiency in running numerous simple operations (such as photon scattering) in parallel [10].

Since the direct propagation of photons even by using GPUs can be extremely time and power consuming, an alternative method is used in IceCube that creates a look-up table that stores the expected timing distribution of photoelectrons at a Digital Optical Module (DOM) for various configurations of the light source and DOM. The concept involves simulating a light source (cascade, track, or flasher) at specific depths and directions multiple times, while tracking the photon yield around the source. Initially, the challenge of creating this table seemed daunting due to the complexity of the problem, as it required a table with 9 dimensions<sup>3</sup>. However, one can take advantage of the approximate horizontal translational and azimuthal symmetry of the ice to reduce the dimensions to 6: depth of the source in ice, zenith angle of the source, displacement vector of the DOM from the source, and time. It is important to note that this approach has its limitations, as it disregards certain effects such as ice layer tilt and anisotropic scattering, which do not adhere to the symmetry assumptions. In recent years, these limitations have been overcome by introducing corrections to scattering lengths (the so-called *effective distance correction*), which was done while developing the double cascade reconstruction [11] that will be explained in Section 1.4, and also by introducing corrections directly in modelling of the ice to account for ice anisotropy and tilt corrections, see Section ?? for details. Initially, Photonics was used to predict and store the expected photon

flux in a multi-dimensional histogram structure, but this method had drawbacks such as binning issues and inaccuracies at great distances. Currently, a more effective approach involves fitting the photoelectron distribution obtained from `CLSim` or `PPC` to a tensor product B-spline surface [12]. This offers the advantage of having a smooth function of all 6 coordinates and can address unphysical fluctuations caused by limited statistics through the use of regularization.

## Detector Simulation

The detector's response is the final step in the simulation process. The PMT's sensitivity depends on the wavelength and angle of the incoming photon, as well as its quantum efficiency. This means that not every photon will trigger the PMT. The simulation takes into account the varying PMT sensitivity for each photon. Additionally, the simulation considers the angular acceptance of photons, accounting for local scattering variations in the ice. The PMT hardware has been thoroughly calibrated and studied in the lab [13], and these results have been incorporated into the simulation. It is important to model the transit time and jitter of the PMT in the simulation, as these factors affect the timing and width of the pulse. Furthermore, all triggers used in real-time data collection at the South Pole are also included in the simulation. This final step in the simulation process completes the creation of a simulated event.

### 1.1.2 SnowStorm Simulation

As described in previous section, specifically for photon propagation stage precise knowledge of ice is important. While we use calibration measurements to estimate the detector properties, this only provides limited precision. When conducting simulations, which are crucial for estimating the detector's response, one need to be careful not to assume specific detector properties. For most of the IceCube analyses so far, variations of the detector response were included using a particular strategy: A set of Monte Carlo simulations with *baseline* values of all systematic parameters was created to estimate event rate in the analysis. The baseline value of a systematic parameter is its most likely value determined from calibration. Variations of this baseline event rate caused by a different, *off-baseline*, detector response were estimated using different *discrete systematics sets*. The combination of discrete baseline and systematics sets allows the estimation of the analysis variables as well as their variation with the detector systematics. This variation is typically assumed to be small and estimated with a low-order Taylor expansion. The off-baseline systematics sets are then used to estimate the coefficients of this expansion.

A new approach to model detector systematic uncertainties has been developed in IceCube, called **SnowStorm Method** [14]. The significant difference compared to the discrete systematics approach described above is that each detector systematic parameter continuously varied while generating the MC events, as visualized in Figure 1.2. Using the SnowStorm method, one obtains a single MC set representing all variations in the detector response. This can help an analysis by reducing the bookkeeping effort necessary for using multiple discrete sets, studying variations in a

[12]: Whitehorn et al. (2013), *Penalized splines for smooth representation of high-dimensional Monte Carlo datasets*

[13]: Abbasi et al. (2010), *Calibration and characterization of the IceCube photomultiplier tube*

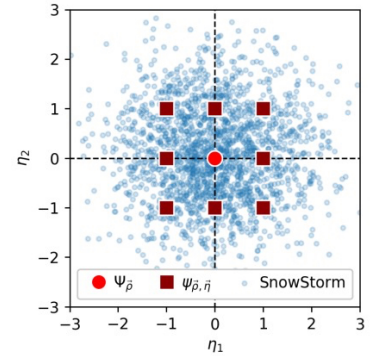


**Figure 1.2:** Illustration of the SnowStorm method described in the text. It depicts the contrast between numerous discrete shifts in nuisance parameters (indicated by red squares), each necessitating an entire Monte Carlo set, in comparison to a single SnowStorm Monte Carlo (represented by small blue dots). Figure taken from [14].

[14]: Aartsen et al. (2019), *Efficient propagation of systematic uncertainties from calibration to analysis with the SnowStorm method in IceCube*



[15]: Ganster (2024), *Measurement of the high-energy astrophysical neutrino energy spectrum combining muon tracks and cascades measured at the IceCube Neutrino Observatory*

[16]: Naab (2024), *Evidence for a Break in the Diffuse Extragalactic Neutrino Spectrum*

[17]: Aartsen et al. (2013), *Evidence for High-Energy Extraterrestrial Neutrinos at the IceCube Detector*

[18]: Abbasi et al. (2021), *IceCube high-energy starting event sample: Description and flux characterization with 7.5 years of data*

[19]: Abbasi et al. (2022), *Detection of astrophysical tau neutrino candidates in IceCube*

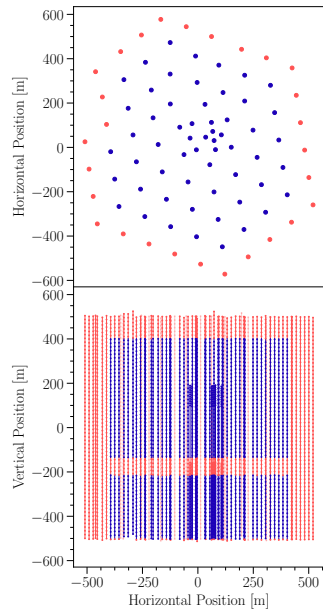


**Figure 1.3:** The top view (above) and side view (below) display the veto DOMs and the DOMs within the fiducial volume for HESE. DOMs highlighted in red represent the veto region, while those in blue define the fiducial volume. Events where the initial detected light comes from the veto region are excluded from the analysis. Figure taken from [18].

large number of detector systematic parameters at once without loss in statistics, and allowing analyses of different event selections to use the same MC set and "marginalize" over all detector systematic parameters that are not relevant for a single analysis.

The analysis presented in this thesis uses simulations generated using this aforementioned novel method. It involves uniform and independent sampling distributions for all relevant parameter uncertainties in the flavour analysis. These simulations cover all three flavours of neutrinos and were created using the SPICE-3.2.1 ice model. They were designed for general use and were also utilized by several other IceCube analyses simultaneously, see [15] and [16] for details. The simulation sets were developed for primary neutrinos in the energy range of  $E_\nu = [100 \text{ GeV} - 1 \text{ PeV}]$  assuming a single power law of  $E_\nu^{-1.5}$ , and in the range  $[1-100 \text{ PeV}]$  with a  $E_\nu^{-1}$  spectrum. The harder spectrum is generally chosen, particularly for higher energy datasets, to ensure a sufficiently large number of events at those energies. Using the weighting method described previously, one can reweight the neutrino events to match any desired spectrum.

## 1.2 High Energy Starting Event (HESE) sample

The High Energy Starting Events (HESE) selection is a comprehensive, all-sky, all-flavour sample of astrophysical and atmospheric neutrinos observed in IceCube. The concept behind HESE is to establish a veto region on the detector's outer edges to select only events where the initial Cherenkov photons are detected inside the fiducial volume. This selection process led to IceCube's first significant milestone: the discovery of an astrophysical neutrino flux [17]. Subsequently, a particle identifier was developed using this sample with added years of data, eventually finding two tau neutrino candidates in IceCube [18, 19]. For the analysis presented in this thesis, this sample was again used, along with some updates in Self-Veto calculations, that shall be introduced in Section 1.2. As shown in Figure 1.3, the veto region includes the outer strings, a top layer of 90 m, a central layer of 80 m around the dust layer, and a 10 m bottom layer. The very thicker veto at the top is essential for filtering out atmospheric muons entering from above. However, the veto can be thinner at the bottom of the detector since up-going atmospheric muons do not exist. The inclusion of a veto around the dust layer is crucial, as horizontal events passing through this highly absorptive region can mimic starting events. To pass the veto, events must deposit fewer than 3 photoelectron (PE) in the veto region out of the first 250 PE recorded within the fiducial volume, and a minimum total charge of 6000 PE is required to ensure high-energy events are selected.

The HESE selection is particularly powerful due to its simplicity, as it does not rely on complex reconstructions, making it robust against changes in filtering or reconstruction algorithms. The fact that it is an all-flavour sample, can help break degeneracies caused by different neutrino flavours producing similar event patterns. Additionally, the all-sky nature of HESE allows for the study of the zenith distribution of events, which can distinguish between atmospheric and astrophysical neutrinos. However, HESE does have limitations: the high-energy threshold introduces uncertainty

in estimating background contributions and astrophysical parameters, and the veto region reduces the detector's effective volume. An extension of HESE to lower energies, known as Medium Energy Starting Events (MESE), has been developed [20] (and recently updated [21]) to overcome some of these limitations.

HESE achieves a significant rejection of atmospheric background while retaining the majority of the astrophysical neutrinos within its fiducial volume. The neutrino effective area of the HESE sample, increases with neutrino energy due to the larger amount of visible light deposited (see Figure 1.4). At energies above a few hundred TeV, the effective areas become similar across all flavours, except the Glashow resonance of  $\bar{\nu}_e$  at 6.3 PeV. However, at lower energies, the effective area varies by flavour due to differences in energy deposition during charged-current interactions, with electron neutrino interactions producing the highest effective area due to the nearly complete energy deposition in electromagnetic and hadronic cascades. For different zenith angles, the effective area decreases as the zenith angle increases, particularly in the up-going region at high energies. This is a result of Earth absorption, which becomes significant for neutrinos above approximately 1 PeV. The distinction between tau neutrinos and other flavours at the highest energies is due to the phenomenon known as **the tau regeneration**, where the tau neutrino regenerates after the decay of a tau lepton [22]. Muon neutrino interactions, on the other hand, produce muons that deposit only part of their energy before escaping the detector, resulting in a higher detection threshold. For  $\nu_\tau$ , the effective areas are between those of  $\nu_\mu$  and  $\nu_e$ .

## Atmospheric Neutrino Self-Veto

As mentioned in Section ??, high-energy cosmic-ray showers produce many neutrinos and muons, which are the only particles able to reach underground detectors such as IceCube. When atmospheric neutrinos reach the detector, they are typically accompanied by other particles from the same CR shower, mostly muons. The chance of a detectable muon to be accompanied by an atmospheric neutrino is called **the atmospheric self-veto probability**. Several things affect this probability, such as the type, energy, and direction of the neutrino. In the case of high-energy CR showers, some muons may reach the detector and *trigger* the veto that marks the event as background. The likelihood of rejecting an atmospheric neutrino through this self-veto mechanism increases with higher neutrino energy and more vertical shower angles. With such a modelling, one effectively suppresses the flux of atmospheric neutrinos, in down-going region<sup>4</sup>. **The passing fraction** of atmospheric neutrinos—defined as the fraction that is not accompanied by a detectable muon from the same CR shower—varies with both neutrino energy and zenith angle [23]. It tends to increase at larger zenith angles, as muons must travel farther through the atmosphere to reach IceCube, as shown in Figure 1.5. At neutrino energies greater than 100 TeV, the contribution from astrophysical neutrinos begins to outweigh the atmospheric background, improving IceCube's ability to detect astrophysical neutrinos as indicate in Figure 1.6.

[20]: Aartsen et al. (2015), *Atmospheric and astrophysical neutrinos above 1 TeV interacting in IceCube*

[21]: Basu et al. (2023), *From PeV to TeV: Astrophysical Neutrinos with Contained Vertices in 10 years of IceCube Data*

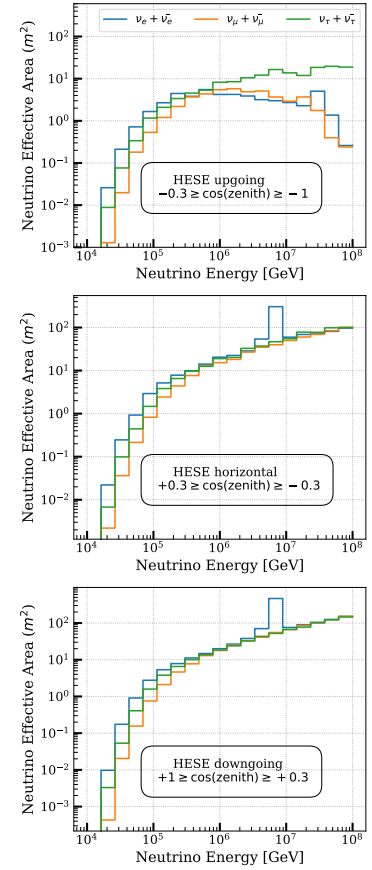


**Figure 1.4:** The neutrino effective areas for the high-energy starting event selection as a function of neutrino energy. The distributions are shown for all neutrino flavours, broken down by various zenith angle ranges.

[22]: Cowen (2007), *Tau neutrinos in IceCube*

4: This process only applies to downward-moving atmospheric neutrinos because muons cannot reach IceCube from below the Earth.

[23]: Argüelles Delgado et al. (2018), *Unified atmospheric neutrino passing fractions for large-scale neutrino telescopes*

[24]: Yuan et al. (n.d.), *nuVeto*

[25]: Fedynitch et al. (2015), *Calculation of conventional and prompt lepton fluxes at very high energy*

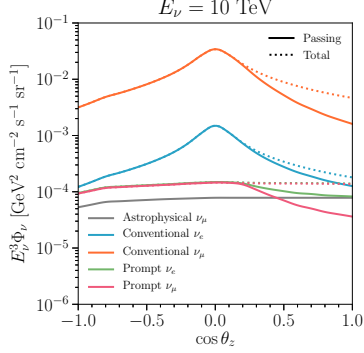


**Figure 1.5:** The Atmospheric neutrino fluxes at  $E_\nu = 10$  TeV. The plot shows the fraction of the flux that is **not** vetoed, known as **passing fluxes** (solid lines), alongside the total flux entering the detector (dashed lines) as a function of the cosine of the zenith angle. Figure is adapted from [23].

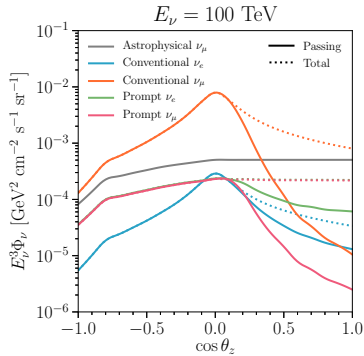


**Figure 1.6:** The atmospheric neutrino fluxes and the effect of self-vetoing are displayed for a neutrino energy level of  $E_\nu = 100$  TeV, see caption of Figure 1.5. Figure atken from [23].

[26]: Aartsen et al. (2014), *Energy Reconstruction Methods in the IceCube Neutrino Telescope*

[12]: Whitehorn et al. (2013), *Penalized splines for smooth representation of high-dimensional Monte Carlo datasets*

[11]: Usner (2018), *Search for Astrophysical Tau-Neutrinos in Six Years of High-Energy Starting Events in the IceCube Detector*

5: to account for the ice layer tilt and anisotropy due to birefringence (see Section ?? for details) separately.

[27]: Yuan (2023), *Detecting neutrinos in IceCube with Cherenkov light in the South Pole ice*

The passing fractions used in the analysis presented in this thesis are based on the calculations derived in [23]. The formalism is similar to the one used in 7.5 years of HESE analysis [18], and it is derived through the *nuVeto* package [24]. The previously used calculations are further updated using MCEq package [25]. MCEq is a tool designed to solve the cascade equations governing cosmic ray-induced showers, allowing for more precise and computationally efficient predictions of atmospheric lepton fluxes.

### 1.3 Maximum Likelihood Event Reconstruction

With the aforementioned HESE sample, next step is to infer the properties of these events—primarily energy, direction, and the deposited light pattern (morphology). To do so, it is necessary to *reconstruct* each individual event. The reconstructed properties are then used to create probability density functions (PDFs) that facilitate likelihood fits for making the desired physics measurements (as outlined in Section ??). Therefore, it is crucial to reconstruct the event properties as accurately as possible. The analysis presented here utilizes a maximum-likelihood estimation (MLE) approach, called *millipede*, for event reconstruction.

*millipede* aims to maximize the likelihood of the observed light pattern from an event, given a specific source hypothesis. The input data comprises individual pulses detected by Digital Optical Modules (DOMs), expressed in terms of charge (measured in photoelectrons (PEs)) and time. These pulses are deconvolved from the digitized waveforms using established single-photoelectron (SPE) pulse templates. The likelihood function compares the observed data to the expected data for a given hypothesis and adjusts the parameters to maximize this likelihood, details of which can be found in [26].

The expected number of photons detected at DOM  $j$  follows a Poisson distribution characterized by a mean  $\lambda_j = \Lambda_j E$ , where  $\Lambda_j$  represents the expected photon yield from a 1 GeV cascade at DOM  $j$ , and  $E$  signifies the cascade's energy, stored in tabulated form as photo splines [12], which were originally developed and used in an analysis similar to the one presented in this thesis [11] and now have been updated\*. with newer ice model<sup>5</sup> [27]. The likelihood of detecting  $k_j$  photons at DOM  $j$  for a cascade with energy  $E$  is given by,

$$L_j = \frac{(E\Lambda_j)^{k_j} e^{-E\Lambda_j}}{k_j!} \quad (1.4)$$

By taking the logarithm and summing over all DOMs, including noise hits  $\rho_j$ , along with an expansion to include multiple light sources  $i$  and timing information, the log-likelihood can be expressed as:

$$\ln L = \sum_{i,j,t} (k_{jt} \ln(E_i \Lambda_{ijt} + \rho_{jt}) - (E_i \Lambda_{ijt} + \rho_{jt}) - \ln(k_{jt}!)) \quad (1.5)$$

\* These updated tables are used in the analysis presented in this thesis



The hypothesis to be compared encompasses the event parameters  $(x_s, y_s, z_s, t_s, \theta_s, \phi_s, E_s)$ , which define the source's location, time, direction, and energy respectively.

`millipede` offers a comprehensive set of configurations that allow users to define how photons are organized in terms of time bins, the magnitude of changes in various parameters, and the exclusion of specific modules from the likelihood calculation. One crucial aspect of these settings is the selection of an ice model for data reconstruction. This model plays a vital role in predicting the expected number of photons that will reach a DOM based on variables such as distance and direction from the source. Additionally, the ice model can influence the timing information of these photons [28], which is critical for accurate event reconstruction. Different approaches to model the ice at the South Pole can significantly affect the reconstructed properties of an event, in particular the double cascade reconstruction using `taupede` (see Section 1.5 at the end of this chapter for such detailed checks). As for exclusions of certain modules, **bright DOMs** and **saturated DOMs** are excluded from the likelihood fit because they may introduce biases by contributing excessively to Equation 1.5. These particular DOMs generally account for a significant portion of the total observed charge. Hence, bright and saturated DOMs along with other DOMs that may have failed during the data acquisition are generally labelled as *Bad DOMs* and are collectively excluded from the reconstruction. `millipede` framework helps reconstruct single and double cascades, along with track source hypotheses. Although they all use the same likelihood from Equation 1.5, they each have different ways to define sources. The hypothesis that fits the observed data best is found by comparing maximum likelihood values, which gives an idea of the interaction type in the detector.

**.monopod:** `monopod` does a simple one-particle cascade energy fit, i.e. it assumes a single light source. It minimizes parameters such as the cascade's deposited energy, neutrino direction (azimuth and zenith), cascade vertex position  $(x, y, z)$ , and vertex time, represented as,  $\vec{h} = (x, y, z, t, \theta, \phi, E)$ . The reconstructed vertex here refers to the shower maximum, which is the peak of the longitudinal energy loss profile and is typically displaced from the interaction vertex by several meters in the considered energy range.

**taupede:** The double cascade fitting algorithm, `taupede`, maximizes the likelihood of two energy depositions with energy  $E_1$  and  $E_2$  respectively, separated by distance  $L_{dc}$ . The second cascade's direction matches the first, and its vertex is determined by the first cascade's vertex, direction, and double cascade length  $L_{dc}$ . The parameters for the double cascade hypothesis are  $\vec{h} = (x_1, y_1, z_1, t_1, \theta, \phi, E_1, L_{dc}, E_2)$ , with the tau traveling in the same direction as the incoming neutrino due to Lorentz boosting. The light yield and timing at each DOM are compared with expected values from the two energy depositions. For the second cascade's timing, the conditions are  $|\vec{x}_2 - \vec{x}_1| = L_{dc}$ ,  $t_2 - t_1 = cL_{dc}$ <sup>6</sup>.

**mumillipede:** Track-like events are parameterized as multiple cascades along its path. The total deposited energy is given by  $E_{dep} = \sum_k E_k$ . Although the deposited energy is not a reliable indicator of the primary neutrino energy, the parameters related to direction and time are vital for neutrino point-source searches.

#### Bright DOM

A Bright DOM generally refers to a situation where a high energy event occurs close to a string, and in first pulse itself, a large amount of charge is observed. This *large amount of charge* is assumed to be 10 times the average observed charge of the event.

#### Saturated DOM

A DOM is considered saturated if its PMT reaches saturation. This can happen if an event occurs close to a string or a very high energy interaction occurs, producing many photons that get collected by the PMT. These DOMs generally do not have *complete* digitized waveforms, making them unsuitable to be used in likelihood based reconstructions.

[28]: Abbasi et al. (2024), *In situ estimation of ice crystal properties at the South Pole using LED calibration data from the IceCube Neutrino Observatory*

#### DeepCore DOM exclusion

DeepCore DOMs have traditionally been excluded from high-energy reconstruction methods like `millipede` because it uses spline tables that assume a uniform single photoelectron (SPE) template for all DOMs. However, the higher quantum efficiency of DeepCore DOMs results in significantly different charge collection, meaning their SPE templates differ from those of other DOMs. Recent efforts have updated simulations to address this issue, and hence they are now included in the reconstructions.

<sup>6</sup>: assuming tau travels through the ice at the speed of light  $c$ .

The algorithm outlined above relies on the quality of the initial hypothesis, also called **seed**. This seed serves as the initial hypothesis  $\vec{h}_0$ . This seed is adjusted until a satisfactory match is achieved between the expected and actual light yield. This process has proven challenging, especially in the case of `taupede`, where the seed combines aspects of both a cascade and a track. Locating an appropriate seed is difficult, and the reconstruction process is influenced by the choice of seed. To reduce this influence, one can either modify the seed or increase the number of iterations; however, both approaches result in greater computational expenses. All algorithms are run multiple times, starting with a provided `seed`, where each subsequent iteration uses the output from the previous one, as explained in Section 1.4. To tackle the challenges associated with reconstructing double cascade events, an improved method for implementing the `taupede` fit was developed [11]. This method effectively converts the fitting process into a *brute-force* approach, where multiple hypotheses are explored and evaluated.

[11]: Usner (2018), *Search for Astrophysical Tau-Neutrinos in Six Years of High-Energy Starting Events in the IceCube Detector*

Simple reconstruction methods like **LineFit** and **SPEFit** provide fast initial estimates for event properties. These methods use limited event information, such as the first photon arrival time or total photoelectrons, without relying on detailed ice properties. The results are then used as seeds for more refined algorithms like `millipede`. For cascade-like events, simpler MLE methods are used to find a charge-weighted mean position of the source, providing an efficient first estimate.

## 1.4 Particle Identification of High Energy Neutrinos

Event reconstruction is performed using the aforementioned `millipede` framework, which enables the identification of different interaction types by assigning a **particle identifier (PID)** to each reconstructed event. The PID provides the probability that an event came from a particular type of interaction. A **ternary topology identifier** has been developed (initially developed in [11] and later used to find first two tau candidates in IceCube [19]) based on the three event topologies—single cascade, double cascade, and track. By using these IDs, Monte Carlo templates are constructed to extract the contribution fractions from each neutrino flavour (see Chapter ??).

[19]: Abbasi et al. (2022), *Detection of astrophysical tau neutrino candidates in IceCube*

This thesis has two main goals: to identify double cascades produced by tau neutrinos and to determine the flavour composition of astrophysical neutrinos. Given the complexity of detecting double cascades and the susceptibility of the reconstruction algorithm to failures and dependence on the initial seed hypothesis, the classification process uses a combination of algorithms offered by the `millipede` framework, which run in parallel on each of the HESE events that provides likelihood for the three event morphologies.

As mentioned before, these methods are *seed* dependent, hence to start with, all selected HESE events are reconstructed using first-guess algorithms to determine their vertex and direction. Result of these quick methods provides an initial fit for the event's position and trajectory, serving as a seed for `monopod`, which performs a fit with four iterations.

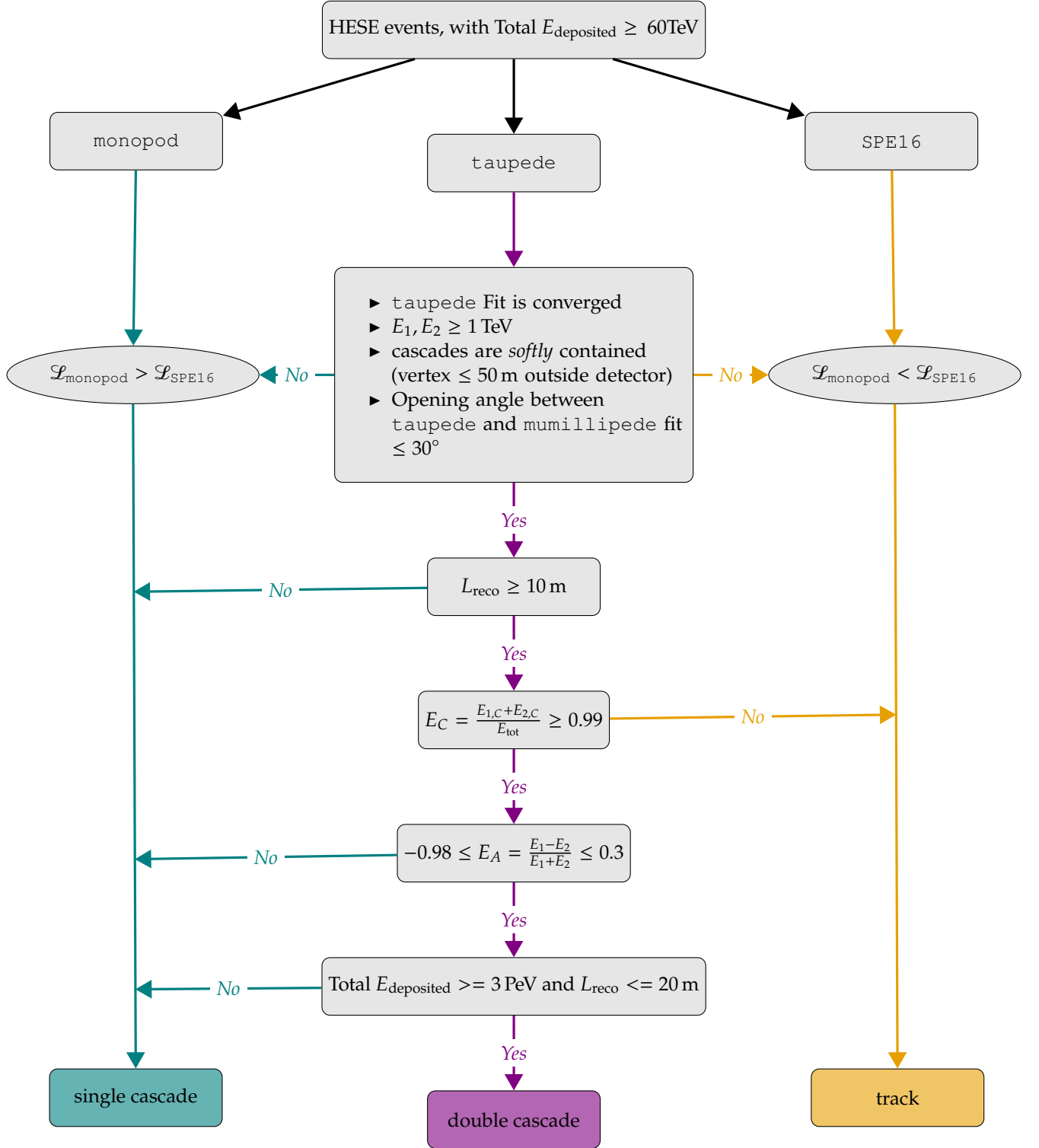


**Figure 1.7:** The event classification scheme for the Ternary PID. All events passing HESE cuts are reconstructed using the three mentioned algorithms. The first level evaluates reconstruction quality; if the criteria are not met, events are classified as single cascades or tracks based on the likelihood values  $L_{\text{monopod}}$  and  $L_{\text{SPE16}}$ . The second level considers the reconstructed length, using a threshold below which distinct vertices of double cascades appear as a single cascade. The third and fourth levels focus on energy confinement and energy asymmetry, respectively. The last level is added to improve purity of the double cascade sample at high energies where misclassification is prominent due to Glashow events.

[11]: Usner (2018), *Search for Astrophysical Tau-Neutrinos in Six Years of High-Energy Starting Events in the IceCube Detector*

7: 4 length seeds shifted 3 times, giving total of 12 seeds.

#### Quality Criteria for $\tau$ aupefit

The final-best fit of  $\tau$ aupefit is accepted only if all the following criteria are satisfied:

- $\tau$ aupefit Fit is converged
- Energies of both of the fitted cascades  $E_1, E_2 \geq 1$  TeV
- Both cascades are *softly* contained (vertex  $\leq 50$  m outside detector)
- Opening angle between  $\tau$ aupefit and mumillipefit  $\leq 30^\circ$

8: If any of the quality checks are fails, the event is assigned track or cascade morphology depending on which of the fit's likelihood is higher.

#### Direction definitions in IceCube

The *zenith angle* ( $\theta$ ) gives the direction of particle origin with respect to the vertical axis that points towards the surface of the ice and upward from the South Pole.

A zenith angle of  $0^\circ$  indicates a particle moving directly downward in the detector,  $90^\circ$  corresponds to horizontal propagation, and  $180^\circ$  signifies a particle moving directly upward.

The *azimuth angle* ( $\phi$ ) gives the direction of particle origin with respect to the horizontal x-axis of the IceCube coordinate system (see Section ??)

Generating a reliable seed for  $\tau$ aupefit is more complex. Multiple seeds are constructed using the monopod fit and generated with varying lengths (10, 25, 50, and 100 meters), each shifted forward, backward, or centered along the direction of the seed in bruce-force way [11]. An amplitude-only  $\tau$ aupefit fit is performed for each of the 12 seeds<sup>7</sup>, and the three best-performing seeds are selected for a full fit, performing 4 iterations of fits again, which incorporates photon arrival times at the DOMs. This method accounts for the diverse photon arrival patterns produced by scattered photons in single energy depositions. The tracks are reconstructed using the SPEFit algorithm, which iteratively (16 times) fits a track based on the first photoelectron detected at each DOM. Although the mumillipefit algorithm could also reconstruct tracks, it is computationally intensive, so SPEFit is preferred. Finally, mumillipefit unfolding is performed along the directions determined by each topology fit (monopod,  $\tau$ aupefit, and SPEFit16), allowing for a comparison of likelihood values for each hypothesis. The best fit is selected for final classification based on the highest likelihood value.

Since identifying tau-induced double cascades is main goal of this process, the comparisons of the three likeelihoods is not the only proxy by which the classifier selects a double cascade event. First, the  $\tau$ aupefit fit is vetted through **Quality Criteria**, on the basis of containment, and reconstructed properties. If these criteria are satisfied<sup>8</sup>, further classification is performed using additional selection criteria based on observables derived from reconstructed quantities, described below.

**The reconstructed direction** of a particle is indicated by its zenith and azimuth angles. The azimuthal angle is not useful for distinguishing between atmospheric and diffuse astrophysical neutrino fluxes since both are isotropically distributed. However, it is important for addressing systematic uncertainties in reconstructed track length due to anisotropic light scattering in the ice. However, zenith angle provides a reliable estimate of the neutrino's initial trajectory, especially for tracks, which can be reconstructed more accurately than cascades.

**The total deposited energy** ( $E_{\text{tot}}$ ) refers to the visible energy in the detector, calculated as the sum of all contained energy losses along the best-fit hypothesis. The total deposited energy serves as a lower limit for neutrino energy and is used as a direct observable in the likelihood fit (see Section ??). Not all energy is deposited in the detector; some may be carried away by secondary neutrinos from tau decays or by muons that leave the detector, while some energy may remain invisible during hadronic showers. Therefore, the sensitivity of total deposited energy to primary neutrino energy varies by event morphology. In single and double cascade topologies, the initial energies of electron and tau neutrinos can be constrained more accurately than those of muon neutrinos, as muon usually leaves the detector and also the energy losses are stochastic, making the proxy weaker.

**The reconstructed length** ( $L_{\text{reco}}$ ), represents the distance between two cascades in double cascade events, is a critical observable for tau-neutrino interactions.

**The energy asymmetry** ( $E_A$ ) measures the distribution of deposited energy between the two cascades in a double cascade event, as illustrated

in Figure 1.8. It is defined as,

$$E_A = \frac{E_1 - E_2}{E_1 + E_2} \quad (1.6)$$

where  $E_1$  and  $E_2$  are reconstructed energies of the first and the second cascades. A *true*<sup>9</sup> single cascade has an energy asymmetry of 1, while a double cascade can have any value between -1 and 1, depending on the kinematics of the neutrino interaction. This variable hence is an excellent estimator to distinguish between a single and a double cascade.

**The energy confinement ( $E_C$ )** measures how much of the total energy is localized near the cascade vertices. It uses the two cascade vertices fitted by `taupede` and deconvolves the energy depositions within 40 m of each of them, as illustrated in Figure 1.9. It is defined as,

$$E_C = \frac{E_{1,c} + E_{2,c}}{E_{\text{tot}}} \quad (1.7)$$

where  $E_{1,c}$  and  $E_{2,c}$  are the deconvolved energy depositions within 40 m distance of first and second cascades respectively and  $E_{\text{tot}}$  is the total deposited energy as defined above. Note that from Equation 1.7,  $E_C = 1$  (with  $E_{1,c} + E_{2,c} = E_1 + E_2 = E_{\text{tot}}$ ) for a  $\nu_\tau$  induced double cascade, as opposed to tracks which have energy depositions outside the region around the double cascade vertices. It is therefore a suitable estimator to separate single cascades and double cascades from tracks.

The classification chain uses several variables to categorize events into three morphologies. If the `taupede` fit meets all the quality criteria, a series of selection cuts is applied. If the event passes all these cuts, it is classified as a double cascade, as illustrated in Figure 1.7. Initially, only high-energy starting events (HESE) with a total energy  $E_{\text{tot}} \geq 60$  TeV are selected to almost entirely eliminate atmospheric muons. If the quality criteria fail based on the likelihood value, the event is assigned either a single cascade or track morphology. The next step ensures that the reconstructed length  $L_{\text{reco}} \geq 10$  m. This condition is necessary because while a double cascade with a length below this threshold could be genuine, the resolution of the reconstruction algorithm does not allow for a definitive classification. Therefore, if the length is below 10 meters, the event is classified as a single cascade. As stated before, cuts on  $E_A$  and  $E_C$  are applied afterwards to further filter out single cascades and tracks from the double cascade samples, respectively. Notably, after the quality cut, it is assumed that the event is a double cascade until any of the selection criteria based on reconstructed properties fail.

A noteworthy point is that none of the events in the HESE sample, with  $E_{\text{tot}} \geq 60$  TeV, are discarded. They are only separated into three sub-samples based on their tagged morphology. All the cuts and selection criteria introduced so far were determined by evaluating the signal-to-background ratio in the distributions of these variables [11]. The cut values were not strictly enforced to allow for some background contribution in the final sample. The rationale behind this selection is that the analysis performed using these three sub-samples is a forward-folding fit (see Section ??). This analysis employs Monte Carlo PDFs that utilize the shapes of signal and background distributions to compare them with data

9: *true* event morphologies are assigned by going through produced charged particles at secondary charged particle propagation stage of the simulation chain (see Section 1.1.1). Looking at the type of particles, their energy depositions and positions within the detector volume, a morphology is assigned to the event.



**Figure 1.8:** A sketch of energy asymmetry, a measure of the relative distribution of total deposited energy between the two cascades, as defined in Equation 1.6. Sketch is adapted from [11].

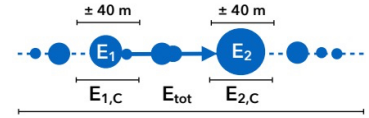


**Figure 1.9:** A sketch of energy confinement, a measure of how confined the reconstructed energy depositions  $E_1$  and  $E_2$  are within 40 m of their reconstructed vertices. Sketch is adapted from [11].

[11]: Usner (2018), *Search for Astrophysical Tau-Neutrinos in Six Years of High-Energy Starting Events in the IceCube Detector*



[11]: Usner (2018), *Search for Astrophysical Tau-Neutrinos in Six Years of High-Energy Starting Events in the IceCube Detector*  
 [29]: Stachurska (2020), *Astrophysical Tau Neutrinos in IceCube*

The Sampling correction here refers to changing the weight of the simulated neutrino, and not changing the HESE sample itself. The weight of a simulated neutrino, as discussed in Section 1.1 takes into account various probabilities, such as interaction type, propagation through earth etc. Most of these probabilities are derived from underlying theoretical models of particle interactions [30]. The correction applied here refers to updates in calculations of these models that affects shape of the underlying cross-section and kinematics of the interactions, that may result in difference in reconstructed variable distributions.

[31]: Glashow (1960), *Resonant Scattering of Antineutrinos*

events. Therefore, it is essential to have a sufficient amount of background simulation present in the sample.

So far, all the explained sample selection and Ternary classification has been applied (with updates in simulations and reconstruction tables) as it was done and used in previous iterations of HESE flavour measurements [11, 29]. For the analysis presented in this thesis, some changes were made both in **sampling** and classification schemes that are discussed in the following subsections.

#### 1.4.1 Reclassification of PeV Double Cascades

The Double Cascade sample is crucial for flavour measurement, necessitating a more comprehensive assessment. Using the ternary classification described, the **flavour purity** of this sample can be determined. Flavour purity is defined as the fraction of a *desired* neutrino flavour within a given morphology sample. This concept is illustrated in Figure 1.10, which displays the reconstructed energy distribution of the Double Cascade sample for each neutrino flavour. Ideally, one would want that each bin in this plot reflects a 100% contribution from the  $\nu_\tau$  flavour. While it does not achieve 100%, it is evident that the Double Cascade sample is predominantly made up of  $\nu_\tau$  events across the energy range. However, a rapid decrease in purity is observed at high energies (around 6 PeV), where the sample becomes dominated by  $\nu_e$  events (see the left panel of Figure 1.10). This shift is due to the Glashow resonance of  $\bar{\nu}_e$ , which significantly influences the cross-section of neutrino interactions at these energies [31]. These events are categorized as Double Cascades because of their high energy deposition over a short distance, but they are misclassified as single cascades.

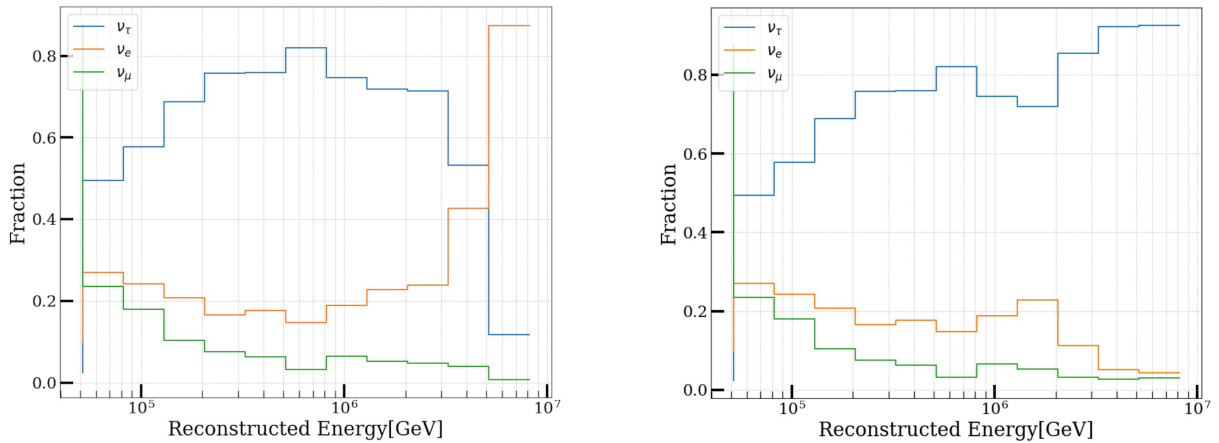


**Figure 1.10:** Fraction of flavour content per bin in double cascade events. The left panel shows the distribution without the criteria of Total  $E_{\text{deposited}} \geq 3$  PeV and  $L_{\text{reco}} \leq 20$  m, indicating *purity contamination* at high energies from  $\bar{\nu}_e$  Glashow events. The right panel presents the distribution after reclassifying double cascades as single cascades under these conditions.

To address this, a **reclassification** mask was introduced at the end of the classification chain outlined in Figure 1.7. If an event is classified as a Double Cascade with a reconstructed energy of  $E_{\text{tot}} \geq 3$  PeV and a reconstructed length  $L_{\text{reco}} \leq 20$  m, it is reclassified as a single cascade. These thresholds were chosen based on the purity distribution to maximize the signal-to-background ratio, even at these energies. The distribution

before and after applying this mask is shown in the left and right panel, of Figure 1.10 respectively. As anticipated, the lower energy distributions remain nearly identical, while purity is restored at higher energies. It is important to note that the fraction of  $\nu_\mu$  remains unchanged in both figures, due to the involvement of only electron neutrinos—technically electron anti-neutrinos—in Glashow interactions, which contribute to the purity contamination. Since this is merely a reclassification, the total High-Energy Starting Event (HESE) sample remains unchanged.

### 1.4.2 Tau Polarisation

As discussed in Section ??, a  $\nu_\tau$ -CC interaction always produces a tau lepton, which has various decay modes. The tau lepton produced in this interaction is polarised, which can significantly alter the kinematics of the tau decay [32, 33]. Whether the decay mode is leptonic or hadronic, the fraction of energy going to the decay products ( $\frac{E_{\text{hadrons/leptons}}}{E_\tau}$ ), is affected if non-zero tau polarisation is not taken into account. The PROPOSAL software used in simulation, to simulate secondary charge particle production, propagation and energy losses does not take into account this factor. That is, the Taus produced in a  $\nu_\tau$ -CC interaction is assumed to be produced with no polarisation. Since the signature which is used for identification of this analysis relies on both, the neutrino interaction cascade and tau decay cascade, not taking in account this correction can lead to an *incomplete* simulation of energy loss profiles. Mainly the energy reconstruction of the second decay cascade may get affected, which can further alter the energy asymmetry ( $E_A$ ) of the event, which is used as a selection variable in Ternary Classifier (see Figure 1.7).

The idea is to test the impact of tau polarisation on analysis variables by reweighting the Monte Carlo events. The calculations provided in [32], are used to get theoretical fractional energy loss of the electromagnetic equivalent visible energy losses, for both polarised and unpolarised states. The ratio of this is multiplied with the simulated fractional energy (which assumed unpolarised taus), to get a new reweighting factor. The change introduced minor difference in the overall observable distributions, hence this was left as a weight correction only and no further analytical checks were performed.

### 1.4.3 Glashow Cross-Section correction

The resonance enhancement of  $\bar{\nu}_e e^-$  scattering at an energy of approximately 6.3 PeV, known as the *Glashow resonance*, was discussed in Section ?. The cross-section for this process at this energy is significantly larger—about two orders of magnitude greater—than that of Deep Inelastic Scattering (DIS). Since this energy range is relevant to the thesis presented in this work, it is crucial to consider second-order QCD corrections, which can significantly alter the Glashow cross-section [34].

The corrections applied to the cross-section, as described in [34], include *Initial State Radiation (ISR)* [35, 36] and the *Doppler broadening effect* [37]. ISR becomes more prominent when the center of mass (COM) energy of the system is much higher than the mass of the initial lepton—since  $W^-$

[32]: Garg et al. (2023), *Neutrino propagation in the Earth and emerging charged leptons with nuPyProp*

[33]: Argüelles et al. (2022), *Tau depolarization at very high energies for neutrino telescopes*

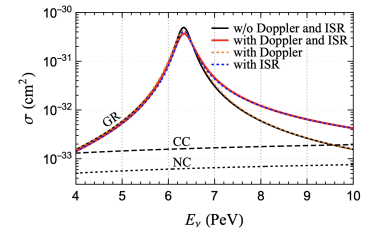


**Figure 1.11:** The cross-section for the Glashow resonance process  $\bar{\nu}_e + e^- \rightarrow W^- \rightarrow X$  is shown with and without initial state radiation and Doppler broadening. The black curve represents the cross-section without these effects, the blue dotted curve includes initial state radiation, the orange dotted curve shows Doppler broadening, and the red curve combines both effects. Figure taken from [34].

[34]: Huang et al. (2023), *Inferring astrophysical neutrino sources from the Glashow resonance*

[35]: Garcia et al. (2020), *Complete predictions for high-energy neutrino propagation in matter*

[36]: Gauld (2019), *Precise predictions for multi-TeV and PeV energy neutrino scattering rates*

[37]: Loewy et al. (2014), *The Effect of Doppler Broadening on the 6.3 PeV  $W^-$  Resonance in  $\bar{\nu}_e e^-$  Collisions*

[26]: Aartsen et al. (2014), *Energy Reconstruction Methods in the IceCube Neutrino Telescope*

[11]: Usner (2018), *Search for Astrophysical Tau-Neutrinos in Six Years of High-Energy Starting Events in the IceCube Detector*

[38]: Chirkin et al. (2013), *Evidence of optical anisotropy of the South Pole ice*

10: Technically it coincides within  $1^\circ$  of the ice flow axis, hence this axis was given a special name, *the anisotropy axis*. The axis along which scattering is reduced is called *the major anisotropy axis* and the one perpendicular to it where scattering is enhanced is known as *the minor anisotropy axis*.

While the SpiceBfr model agrees much better with the data, compared to Spice-3.2.1, it is important to note that on the analysis level, where one uses reconstruction algorithms based on all of the pulse information from the DOMs, the ever so significant effect on charge and time level may get smeared off from overall observable distributions. Going from Spice-mie to Spice-Lea was a breakthrough as the former did not consider this anisotropic behavior of photon propagation. The transition from Spice-3.2.1 to Spice-Bfr represented a shift toward directly modeling the intrinsic properties of the ice crystals to account for anisotropy. In contrast, Spice-3.2.1 and Spice-Lea employed an approximated approach, simulating anisotropic photon scattering as an effective solution. ximated solution in the form of effectively mimicking an anisotropic scattering of photons.

is substantially more massive than  $e^-$ , this leads to an enhancement factor of approximately  $\frac{M_W}{m_e} \sim 12$  in cross-section, on top of contributions from the fine structure constant ( $\alpha$ ) as shown in Figure 1.11, blue dotted line. This results in collinear photon emission. Doppler broadening occurs due to the motion of atomic electrons, where the typical velocity of the electron is assumed to be close to the speed of light. This motion causes the COM energy to shift by a factor of  $(1 - \beta \cos \theta)$ , where  $\theta$  is the angle between the electron's velocity ( $\beta$ ) and the incoming neutrino in the lab frame [37].

The combined results of these effects, based on calculations from [34], were used to adjust the *total weight* of neutrinos. As noted in [34], these effects are smoothed out by the energy resolution of IceCube [26], and the impact of this reweighting on energy distributions and sensitivity was negligible. Nevertheless, the reweighting was retained, similar to the correction for Tau polarization.

## 1.5 Influence of South Pole Ice properties on Double Cascades Reconstruction

The identification of  $\nu_\tau$ -induced double cascades in the IceCube detector faces significant systematic uncertainties due to the anisotropy of the ice. As discussed in Section ??, the Anisotropy at the South Pole ice has been established since 2013 [38]. This phenomenon causes photons to have a directional dependence while scattering, with enhanced scattering occurring perpendicular to the ice flow axis<sup>10</sup> and reduced scattering along it.

Such a direction dependent scattering pattern can cause a bias in reconstructing specifically a double cascade event using *taupede*, as this algorithm looks for energy depositions around vertices along a given seed direction (see Section 1.4), which can cause bias in length reconstruction. When a single cascade aligns with this major anisotropy axis, reduced scattering can elongate its apparent size, mimicking double cascade characteristics due to altered light timing at the DOMs. Conversely, if a true double cascade aligns with one of the minor anisotropy axes, it may be compressed, increasing the risk of misidentification as a single cascade. Without accounting for anisotropy, true single cascades could be misclassified as double cascades, while genuine double cascades along minor axes might be missed.

Reconstructing these events relies on photo-spline tables introduced in Section 1.3, which provide tabulated light yields for simulated 1 GeV cascades. These cascades are placed in the detector's center at intervals of  $\Delta z = 20$  m, between depths of  $-600$  to  $600$  m and zenith angles from  $0^\circ$  to  $180^\circ$ . The initial model primarily considers the ice layer's depth and zenith angle for light propagation, but an additional azimuthal dimension was necessary to account for anisotropy. A key advancement was the development of **the effective distance spline tables**, which adjusted for anisotropy by using an isotropic-ice-equivalent position instead of position of the DOMs to look-up for the light yield, which resulted in a significant enhancing of length reconstruction accuracy [11].



**Table 1.1:** The four comparison scenarios that were analyzed. The first column refers to the name of the combination being tested, with ice model in the name always refers to the one used in simulation. The second and third column is ice model used in simulation and reconstruction respectively. Last column points to corresponding figures.

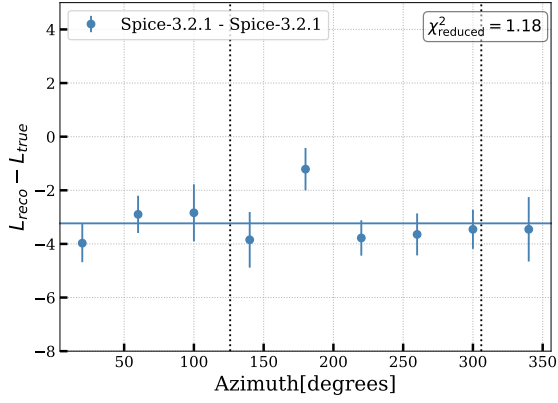
Name	Simulation ice model	Reconstruction ice model	
Spice-3.2.1-Spice-3.2.1	Spice-3.2.1	Spice-3.2.1	Figure 1.12a
Spice-3.2.1-SpiceBfr	Spice-3.2.1	SpiceBfr	Figure 1.12b
SpiceBfr-Spice-3.2.1	SpiceBfr	Spice-3.2.1	Figure 1.12c
SpiceBfr-SpiceBfr	SpiceBfr	SpiceBfr	Figure 1.12d

Recent developments in ice model studies have revealed that the directional behavior of light in ice is due to its molecular structure, a phenomenon known as *birefringence*, as already introduced in Section ?? . This is now incorporated into the new ice model, called, **SpiceBfr**. However, during the development stage of the analysis presented in this thesis, the only large-scale Monte Carlo simulations available were the one produced using an earlier ice model, **Spice-3.2.1**<sup>11</sup>. Naturally, the question arises, if SpiceBfr can further improve reconstruction (or discover any previously unknown biases), hence a comparison was needed.

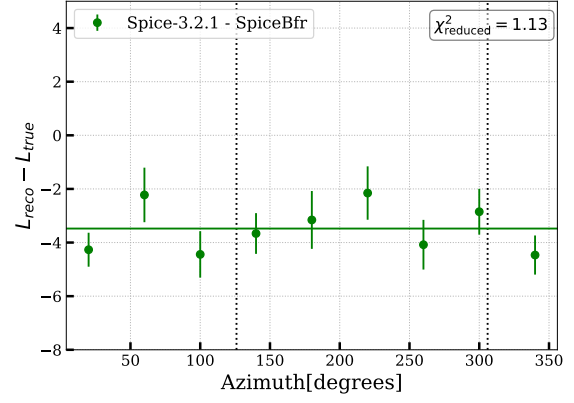
11: This ice model is almost identical to the one used in previous the iteration of this analysis [29]

Such a check between Spice-3.2.1 and SpiceBfr was feasible since the spline tables for SpiceBfr were already available. To facilitate cross-comparison, a small statistics (one-third of the full available statistics) simulation set was produced using SpiceBfr. All the tested combinations are listed in Table 1.1. The successfully identified true double cascades are considered, and median length bias ( $L_{\text{Reco}} - L_{\text{true}}$ ) is calculated per azimuth bin (see Figure 1.12). An effective reconstruction algorithm should show no bias (i.e. the difference in length should be zero), unless unaccounted asymmetries exist.

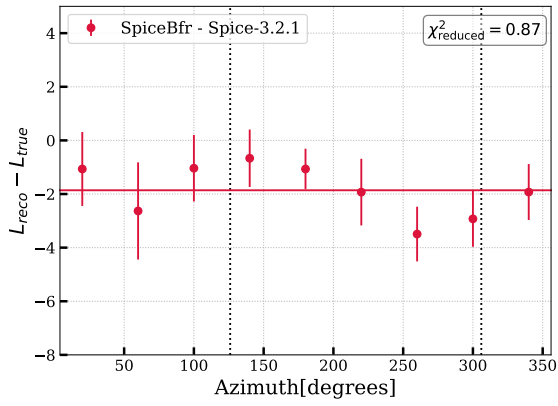
Since all cases involve either the effective distance correction or an inherent anisotropy parametrization (via birefringence), minimal bias was expected along the major anisotropy axis. As shown in the results, only minor structures were observed, and none were deemed statistically significant, particularly along the anisotropy axis. To probe further, a  $\chi^2$  goodness-of-fit (gof) test was performed to fit a horizontal line, with the reduced  $\chi^2$  calculated for each of the four cases (values indicated on all figures). The results indicated that all four combinations fit well to a horizontal line, signifying no significant biases were present. However, the plots corresponding to the simulation produced using SpiceBfr (both reconstructed with SpiceBfr (Figure 1.12d) and Spice-3.2.1 Figure 1.12c) showed signs of over/underfitting, likely due to the low statistics of the generated SpiceBfr simulation set.



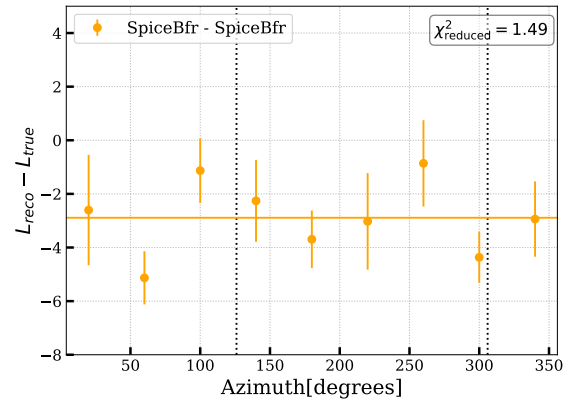
(a) Simulation using Spice-3.2.1 and reconstruction using Spice-3.2.1



(b) Simulation using Spice-3.2.1 and reconstruction using SpiceBfr



(c) Simulation using SpiceBfr and reconstruction using Spice-3.2.1



(d) Simulation using SpiceBfr and reconstruction using SpiceBfr

**Figure 1.12:** The length bias of true double cascades, classified as double cascades, as function of Azimuth angle. Vertical lines show the direction of the major anisotropy axis. The caption of each panel states the combination of icemodels used. Each figure also shows reduced value of  $\chi^2$  calculated by fitting the shown horizontal line, see text for details.

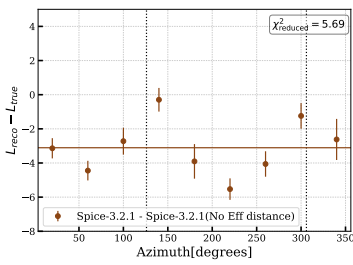


**Figure 1.13:** Simulation using Spice-3.2.1 and reconstruction using Spice-3.2.1 but no effective distance. See caption of Figure 1.12 for details.

This observed lack of bias aligns with expectations, as Spice-3.2.1 effectively handles anisotropy through the effective distance parametrization. The final step thus, was to verify if the lack of bias was truly due to the effective distance splines. In Figure 1.13, a distribution is shown where events are simulated using Spice-3.2.1 but reconstructed without the effective distance correction. The resulting reduced  $\chi^2$  of 5.69 indicates a poor fit, and a clear bias is visible along the anisotropy axis, as was observed in [11]. This conclusively demonstrates that both Spice-3.2.1 and SpiceBfr, both with appropriate effective distance corrections are well-suited for analyzing  $\nu_\tau$ -induced double cascades in the presence of ice anisotropy.

Given that the SpiceBfr model represents the best current understanding of the South Pole ice, the decision was made **to proceed with Spice-3.2.1 simulations reconstructed using the SpiceBfr model**. This approach is further supported by the reduced  $\chi^2$  values across the four cases, with the Spice-3.2.1 simulation and SpiceBfr reconstruction yielding the value closest to 1, indicating the most accurate fit.

# APPENDIX



# List of Figures

1.1	Light emission pattern of a simulated muon track event, using the direction propagation program CLSim. The colored lines show individual photon paths through ice, with red indicating earlier and blue indicating later compared to an unscattered photon. Figure taken from [9]. . . . .	4
1.2	Illustration of the SnowStorm method described in the text. It depicts the contrast between numerous discrete shifts in nuisance parameters (indicated by red squares), each necessitating an entire Monte Carlo set, in comparison to a single SnowStorm Monte Carlo (represented by small blue dots). Figure taken from [14]. . . . .	5
1.3	The top view (above) and side view (below) display the veto DOMs and the DOMs within the fiducial volume for HESE. DOMs highlighted in red represent the veto region, while those in blue define the fiducial volume. Events where the initial detected light comes from the veto region are excluded from the analysis. Figure taken from [18]. . . . .	6
1.4	The neutrino effective areas for the high-energy starting event selection as a function of neutrino energy. The distributions are shown for all neutrino flavours, broken down by various zenith angle ranges. . . . .	7
1.5	The Atmospheric neutrino fluxes at $E_\nu = 10$ TeV. The plot shows the fraction of the flux that is <b>not</b> vetoed, known as <b>passing fluxes</b> (solid lines), alongside the total flux entering the detector (dashed lines) as a function of the cosine of the zenith angle. Figure is adapted from [23]. . . . .	8
1.6	The atmospheric neutrino fluxes and the effect of self-vetoing are displayed for a neutrino energy level of $E_\nu = 100$ TeV, see caption of Figure 1.5. Figure atken from [23]. . . . .	8
1.7	The event classification scheme for the Ternary PID. All events passing HESE cuts are reconstructed using the three mentioned algorithms. The first level evaluates reconstruction quality; if the criteria are not met, events are classified as single cascades or tracks based on the likelihood values $L_{\text{monopod}}$ and $L_{\text{SPE16}}$ . The second level considers the reconstructed length, using a threshold below which distinct vertices of double cascades appear as a single cascade. The third and fourth levels focus on energy confinement and energy asymmetry, respectively. The last level is added to improve purity of the double cascade sample at high energies where misclassification is prominent due to Glashow events. . . . .	11
1.8	A sketch of energy asymmetry, a measure of the relative distribution of total deposited energy between the two cascades, as defined in Equation 1.6. Sketch is adapted from [11]. . . . .	13
1.9	A sketch of energy confine- ment, a measure of how confined the reconstructed energy depositions E1 and E2 are within 40 m of their reconstructed vertices. Sketch is adapted from [11]. . . . .	13
1.10	Fraction of flavour content per bin in double cascade events. The left panel shows the distribution without the criteria of Total $E_{\text{deposited}} \geq 3$ PeV and $L_{\text{reco}} \leq 20$ m, indicating <i>purity contamination</i> at high energies from $\bar{\nu}_e$ Glashow events. The right panel presents the distribution after reclassifying double cascades as single cascades under these conditions. . . . .	14
1.11	The cross-section for the Glashow resonance process $\nu_e + e^- \rightarrow W^- \rightarrow X$ is shown with and without initial state radiation and Doppler broadening. The black curve represents the cross-section without these effects, the blue dotted curve includes initial state radiation, the orange dotted curve shows Doppler broadening, and the red curve combines both effects. Figure taken from [34]. . .	15
1.12	The length bias of true double cascades, classified as double cascades, as function of Azimuth angle. Vertical lines show the direction of the major anisotropy axis. The caption of each panel states the combination of icemodels used. Each figure also shows reduced value of $\chi^2$ calculated by fitting the shown horizontal line, see text for details. . . . .	18
1.13	Simulation using Spice-3.2.1 and reconstruction using Spice-3.2.1 but no effective distance. See caption of Figure 1.12 for details. . . . .	18



# List of Tables

- 1.1 The four comparison scenarios that were analyzed. The first column refers to the name of the combination being tested, with ice model in the name always refers to the one used in simulation. The second and third column is ice model used in simulation and reconstruction respectively. Last column points to corresponding figures. . . . . 17





# Bibliography

Here are the references in citation order.

- [1] A. Gazizov and M. P. Kowalski. “ANIS: High energy neutrino generator for neutrino telescopes”. In: *Comput. Phys. Commun.* 172 (2005), pp. 203–213. doi: [10.1016/j.cpc.2005.03.113](https://doi.org/10.1016/j.cpc.2005.03.113) (cited on page 2).
- [2] D. Heck et al. “CORSIKA: A Monte Carlo code to simulate extensive air showers”. In: (Feb. 1998) (cited on page 2).
- [3] J. van Santen. “Neutrino Interactions in IceCube above 1 TeV: Constraints on Atmospheric Charmed-Meson Production and Investigation of the Astrophysical Neutrino Flux with 2 Years of IceCube Data taken 2010–2012”. PhD thesis. Wisconsin U., Madison, Nov. 2014 (cited on page 2).
- [4] J. H. Koehne et al. “PROPOSAL: A tool for propagation of charged leptons”. In: *Comput. Phys. Commun.* 184 (2013), pp. 2070–2090. doi: [10.1016/j.cpc.2013.04.001](https://doi.org/10.1016/j.cpc.2013.04.001) (cited on page 3).
- [5] D. Chirkin and W. Rhode. “Propagating leptons through matter with Muon Monte Carlo (MMC)”. In: (Aug. 2004) (cited on page 3).
- [6] B. Voigt. “Sensitivity of the IceCube detector for ultra-high energy electron-neutrino events”. PhD thesis. Humboldt-Universität zu Berlin, Mathematisch-Naturwissenschaftliche Fakultät I, 2008. doi: [http://dx.doi.org/10.18452/15850](https://dx.doi.org/10.18452/15850) (cited on page 4).
- [7] L. Rädcl and C. Wiebusch. “Calculation of the Cherenkov light yield from electromagnetic cascades in ice with Geant4”. In: *Astropart. Phys.* 44 (2013), pp. 102–113. doi: [10.1016/j.astropartphys.2013.01.015](https://doi.org/10.1016/j.astropartphys.2013.01.015) (cited on page 4).
- [8] L. Rädcl and C. Wiebusch. “Calculation of the Cherenkov light yield from low energetic secondary particles accompanying high-energy muons in ice and water with Geant 4 simulations”. In: *Astroparticle Physics* 38 (June 2012) (cited on page 4).
- [9] C. Kopper. *Photons from IceCube Muon*. URL: <https://www.psu.edu/news/research/story/national-science-foundation-funds-supercomputer-cluster-penn-state> (cited on page 4).
- [10] D. Chirkin. “Photon tracking with GPUs in IceCube”. In: *Nuclear Instruments and Methods in Physics Research Section A: Accelerators, Spectrometers, Detectors and Associated Equipment* 725 (2013), pp. 141–143. doi: <https://doi.org/10.1016/j.nima.2012.11.170> (cited on page 4).
- [11] M. Usner. “Search for Astrophysical Tau-Neutrinos in Six Years of High-Energy Starting Events in the IceCube Detector”. PhD thesis. Humboldt-Universität zu Berlin, Mathematisch-Naturwissenschaftliche Fakultät, 2018. doi: [http://dx.doi.org/10.18452/19458](https://dx.doi.org/10.18452/19458) (cited on pages 4, 8, 10, 12–14, 16, 18).
- [12] N. Whitehorn, J. van Santen, and S. Lafebre. “Penalized splines for smooth representation of high-dimensional Monte Carlo datasets”. In: *Computer Physics Communications* 184.9 (2013), pp. 2214–2220. doi: <https://doi.org/10.1016/j.cpc.2013.04.008> (cited on pages 5, 8).
- [13] R. Abbasi et al. “Calibration and characterization of the IceCube photomultiplier tube”. In: *Nuclear Instruments and Methods in Physics Research Section A: Accelerators, Spectrometers, Detectors and Associated Equipment* 618.1 (2010), pp. 139–152. doi: <https://doi.org/10.1016/j.nima.2010.03.102> (cited on page 5).
- [14] M. G. Aartsen et al. “Efficient propagation of systematic uncertainties from calibration to analysis with the SnowStorm method in IceCube”. In: *JCAP* 10 (2019), p. 048. doi: [10.1088/1475-7516/2019/10/048](https://doi.org/10.1088/1475-7516/2019/10/048) (cited on page 5).
- [15] E. Ganster. “Measurement of the high-energy astrophysical neutrino energy spectrum combining muon tracks and cascades measured at the IceCube Neutrino Observatory”. PhD thesis. RWTH Aachen University, RWTH Aachen U., 2024 (cited on page 6).

- [16] R. Naab. “Evidence for a Break in the Diffuse Extragalactic Neutrino Spectrum”. PhD thesis. Humboldt-Universität zu Berlin, Mathematisch-Naturwissenschaftliche Fakultät, 2024 (cited on page 6).
- [17] M. G. Aartsen et al. “Evidence for High-Energy Extraterrestrial Neutrinos at the IceCube Detector”. In: *Science* 342.6161 (2013), p. 1242856. doi: [10.1126/science.1242856](https://doi.org/10.1126/science.1242856) (cited on page 6).
- [18] R. Abbasi et al. “IceCube high-energy starting event sample: Description and flux characterization with 7.5 years of data”. In: *Physical Review D* 104.2 (2021). doi: [10.1103/PhysRevD.104.022002](https://doi.org/10.1103/PhysRevD.104.022002) (cited on pages 6, 8).
- [19] R. Abbasi et al. “Detection of astrophysical tau neutrino candidates in IceCube”. In: *The European Physical Journal C* 82.11 (2022). doi: [10.1140/epjc/s10052-022-10795-y](https://doi.org/10.1140/epjc/s10052-022-10795-y) (cited on pages 6, 10).
- [20] M. G. Aartsen et al. “Atmospheric and astrophysical neutrinos above 1 TeV interacting in IceCube”. In: *Phys. Rev. D* 91 (2 Jan. 2015), p. 022001. doi: [10.1103/PhysRevD.91.022001](https://doi.org/10.1103/PhysRevD.91.022001) (cited on page 7).
- [21] V. Basu et al. “From PeV to TeV: Astrophysical Neutrinos with Contained Vertices in 10 years of IceCube Data”. In: *PoS ICRC2023* (2023), p. 1007. doi: [10.22323/1.444.1007](https://doi.org/10.22323/1.444.1007) (cited on page 7).
- [22] D. F. Cowen. “Tau neutrinos in IceCube”. In: *J. Phys. Conf. Ser.* 60 (2007). Ed. by F. Halzen, A. Karle, and T. Montaruli, pp. 227–230. doi: [10.1088/1742-6596/60/1/048](https://doi.org/10.1088/1742-6596/60/1/048) (cited on page 7).
- [23] C. Argüelles Delgado et al. “Unified atmospheric neutrino passing fractions for large-scale neutrino telescopes”. In: *Journal of Cosmology and Astroparticle Physics* 2018 (July 2018), pp. 047–047. doi: [10.1088/1475-7516/2018/07/047](https://doi.org/10.1088/1475-7516/2018/07/047) (cited on pages 7, 8).
- [24] T. Yuan et al. *nuVeto*. URL: <https://github.com/tianluyuan/nuVeto> (cited on page 8).
- [25] A. Fedynitch et al. “Calculation of conventional and prompt lepton fluxes at very high energy”. In: *EPJ Web Conf.* 99 (2015). Ed. by D. Berge et al., p. 08001. doi: [10.1051/epjconf/20159908001](https://doi.org/10.1051/epjconf/20159908001) (cited on page 8).
- [26] M. G. Aartsen et al. “Energy Reconstruction Methods in the IceCube Neutrino Telescope”. In: *JINST* 9 (2014), P03009. doi: [10.1088/1748-0221/9/03/P03009](https://doi.org/10.1088/1748-0221/9/03/P03009) (cited on pages 8, 16).
- [27] T. Yuan. “Detecting neutrinos in IceCube with Cherenkov light in the South Pole ice”. In: *Nucl. Instrum. Meth. A* 1054 (2023), p. 168440. doi: [10.1016/j.nima.2023.168440](https://doi.org/10.1016/j.nima.2023.168440) (cited on page 8).
- [28] R. Abbasi et al. “In situ estimation of ice crystal properties at the South Pole using LED calibration data from the IceCube Neutrino Observatory”. In: *The Cryosphere* 18.1 (2024), pp. 75–102. doi: [10.5194/tc-18-75-2024](https://doi.org/10.5194/tc-18-75-2024) (cited on page 9).
- [29] J. Stachurska. “Astrophysical Tau Neutrinos in IceCube”. PhD thesis. Humboldt-Universität zu Berlin, Mathematisch-Naturwissenschaftliche Fakultät, 2020. doi: <http://dx.doi.org/10.18452/21611> (cited on pages 14, 17).
- [30] A. Cooper-Sarkar, P. Mertsch, and S. Sarkar. “The high energy neutrino cross-section in the Standard Model and its uncertainty”. In: *JHEP* 08 (2011), p. 042. doi: [10.1007/JHEP08\(2011\)042](https://doi.org/10.1007/JHEP08(2011)042) (cited on page 14).
- [31] S. L. Glashow. “Resonant Scattering of Antineutrinos”. In: *Phys. Rev.* 118 (1 Apr. 1960), pp. 316–317. doi: [10.1103/PhysRev.118.316](https://doi.org/10.1103/PhysRev.118.316) (cited on page 14).
- [32] D. Garg et al. “Neutrino propagation in the Earth and emerging charged leptons with nuPyProp”. In: *JCAP* 01 (2023), p. 041. doi: [10.1088/1475-7516/2023/01/041](https://doi.org/10.1088/1475-7516/2023/01/041) (cited on page 15).
- [33] C. A. Argüelles et al. “Tau depolarization at very high energies for neutrino telescopes”. In: *Phys. Rev. D* 106.4 (2022), p. 043008. doi: [10.1103/PhysRevD.106.043008](https://doi.org/10.1103/PhysRevD.106.043008) (cited on page 15).
- [34] G.-y. Huang, M. Lindner, and N. Volmer. “Inferring astrophysical neutrino sources from the Glashow resonance”. In: *JHEP* 11 (2023), p. 164. doi: [10.1007/JHEP11\(2023\)164](https://doi.org/10.1007/JHEP11(2023)164) (cited on pages 15, 16).
- [35] A. Garcia et al. “Complete predictions for high-energy neutrino propagation in matter”. In: *JCAP* 09 (2020), p. 025. doi: [10.1088/1475-7516/2020/09/025](https://doi.org/10.1088/1475-7516/2020/09/025) (cited on page 15).
- [36] R. Gauld. “Precise predictions for multi-TeV and PeV energy neutrino scattering rates”. In: *Phys. Rev. D* 100.9 (2019), p. 091301. doi: [10.1103/PhysRevD.100.091301](https://doi.org/10.1103/PhysRevD.100.091301) (cited on page 15).

- [37] A. Loewy, S. Nussinov, and S. L. Glashow. “The Effect of Doppler Broadening on the 6.3  $PeV$   $W^-$  Resonance in  $\bar{\nu}_e e^-$  Collisions”. In: (July 2014) (cited on pages 15, 16).
- [38] D. Chirkin and IceCube Collaboration. “Evidence of optical anisotropy of the South Pole ice”. In: *International Cosmic Ray Conference*. Vol. 33. International Cosmic Ray Conference. Jan. 2013, p. 3338 (cited on page 16).